

Supersonically Sprayed $Zn_2SnO_4/SnO_2/CNT$ Nanocomposites for High-Performance Supercapacitor Electrodes

Edmund Samuel,^{†,‡,§,ID} Tae-Gun Kim,^{†,‡} Chan-Woo Park,[†] Bhavana Joshi,[†] Mark T. Swihart,^{§,ID} and Sam S. Yoon^{*,†,‡,ID}

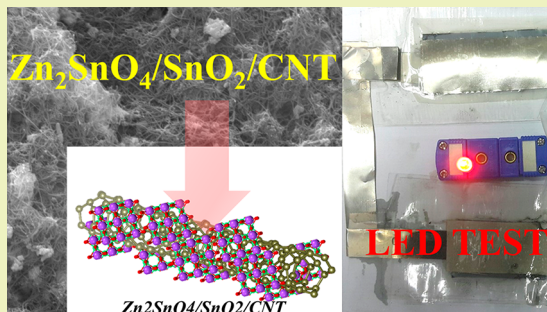
[†]School of Mechanical Engineering, Korea University, Seoul, 02841, Republic of Korea

[§]Department of Chemical & Biological Engineering and RENEW Institute, University at Buffalo, The State University of New York, Buffalo, New York 14260-4200, United States

Supporting Information

ABSTRACT: In this study, we demonstrate rapid and facile supersonic cold spray deposition of $Zn_2SnO_4/SnO_2/CNT$ nanocomposite supercapacitor electrodes with promising combinations of power and energy density. Cyclic voltammetry confirmed the capacitive behavior of the optimized electrode, with specific capacitance reaching $260 \text{ F}\cdot\text{g}^{-1}$ at a current density of $10 \text{ A}\cdot\text{g}^{-1}$. We attribute this high performance to the optimal combination of CNT (carbon nanotube; double-layer capacitance) and Zn_2SnO_4/SnO_2 (pseudocapacitance) properties. The mesoporous and accessible surface of the CNT significantly contributed to the excellent retention (approximately 93%) of the specific capacitance after 15000 galvanostatic charge/discharge cycles. In addition, the supercapacitor exhibited a remarkable energy density, electrochemical properties, and mechanical stability. The materials and approach presented here can enable cost-effective, efficient, and scalable production of high-performance supercapacitor electrodes.

KEYWORDS: Cold spray technique, Supercapacitor, Zn_2SnO_4 , CNT, Nanocomposite



INTRODUCTION

Rapid economic development based on increased use of nonrenewable fossil fuels has driven climate change and led to many types of pollution that harm the environment. Major changes in patterns of energy production and utilization will be required to avoid catastrophic effects.^{1–3} Alternative and inexpensive renewable and clean energy sources are needed to solve this environmental and energy crisis.⁴ Electrical energy storage devices such as lithium-ion batteries and supercapacitors are needed for the effective use of solar and wind energy, which are inherently intermittent sources. Harnessing renewable electricity for transportation requires portable energy storage with high gravimetric and volumetric power and energy densities. Compared to lithium-ion batteries, the higher power density, faster charging ability, and longer life cycle of supercapacitors (SCs) make them valuable components of many energy storage systems.^{5,6} However, SCs generally have lower energy density than lithium-ion batteries and can be prone to self-discharge.

The capacitance of a supercapacitor arises from two different basic mechanisms: electrochemical double-layer capacitance (EDLC) and pseudocapacitance.^{7–10} EDLC occurs due to the separation of electric charges at the electrode/electrolyte interface with the electrostatic adsorption/desorption of ions in the absence of Faradaic reactions.¹¹ In contrast to EDLC, pseudocapacitance involves Faradaic reactions. Supercapacitors

based on reducible metal oxides (pseudocapacitive materials) can exhibit much higher energy density than those based on only EDLC.¹² However, charge/discharge rates in these devices are limited by the rates of the Faradaic reactions.

Most transition metal oxides (TMOs) have excellent reversible reduction and oxidation reaction characteristics. In particular, ruthenium oxide is an excellent pseudocapacitive material, but its use is limited due to its toxicity, scarcity, and high cost.¹³ TMOs, such as manganese oxide, iron oxide, tin oxide, zinc oxide, and cerium oxide, are preferred owing to their low cost and low toxicity combined with high specific capacitance and power density.^{14–18} In each of these cases, the TMO framework contains a multivalent metal that cycles between oxidation states. This requires the diffusion of electrolyte and ions outside and within the TMO framework, respectively. The rates of these redox reactions are often hindered by large activation barriers for ionic mobility.¹⁹ Thus, energy density is often limited by the concentration of redox-active sites, whereas power density is often limited by the rate of ion diffusion.

Most TMOs are also electrically insulating. Their performance can be increased by adding an electronically conductive

Received: May 7, 2019

Revised: June 17, 2019

Published: July 18, 2019

material, preferably one with a high surface area to provide EDLC.^{20,21} Various combinations of conductive carbon materials with TMOs have been studied. Lee et al.²² reported a gravimetric energy density of 15.8 Wh·kg⁻¹ for CNF/graphene/MnO₂, and Li et al.²³ demonstrated a MnO₂/SCNT (single-walled carbon nanotube) solid-state supercapacitor with a volumetric energy density of 10.4 mWh·cm⁻³. Shi et al.²⁴ reported a high-performance Co₃O₄@carbon fiber@Co₃O₄ supercapacitor with a specific energy density and power density of 57.4 Wh·kg⁻¹ and 375 W·kg⁻¹, respectively. Fe₃O₄-doped double-shelled hollow carbon spheres reported by Li et al. delivered an energy density and power density of 45 Wh·kg⁻¹ and 400 W·kg⁻¹, respectively, and 96.7% retention of the specific capacitance after 8000 cycles.²⁵

Recently, mixed-metal oxides incorporating two different multivalent cations, with a spinel crystal structure and stoichiometry of A_xB_{3-x}O₄, where A and B are elements such as copper, magnesium, zinc, iron, nickel, and titanium, have emerged as promising supercapacitor electrode materials. Bimetallic oxides such as Zn₂SnO₄ can increase electrochemical energy storage by supporting multielectron redox reactions at different potentials.^{26–28} Bimetallic oxides can change structure during the Faradaic reactions, providing an additional degree of freedom and facilitating rapid ion diffusion.²⁹ In addition, self-matrices alleviate agglomeration during calcination and provide better thermal stability, while the multivalent cations deliver more electrochemical sites.^{28,30–32}

In this study, the electrochemical performance of a Zn₂SnO₄/SnO₂/CNT composite was evaluated as a supercapacitor electrode. Nanostructured films of the Zn₂SnO₄/SnO₂/CNT composite were deposited by supersonic cold spraying. The fast and scalable cold spray deposition provided excellent adhesion to the substrate, due to the high-speed impact of particles. The additional benefits of cold spray deposition are discussed in our previous studies.³³ The grafting of Zn₂SnO₄/SnO₂ particles over CNT occurred directly due to the supersonic impact. Relative to alternative methods, the cold spray approach eliminates several steps, such as particle growth over CNT and washing of such CNT/metal oxide composites to remove undesirable contamination in techniques such as hydrothermal synthesis and chemical precipitation. The nano/submicrometer particles of Zn₂SnO₄/SnO₂ provided short diffusion pathways that improved the charge-transfer capability of composites. The high specific capacitance, long life cycle, and enhanced energy and power densities of the electrodes produced using this cold spray method demonstrate the potential of the Zn₂SnO₄/SnO₂/CNT composite as a supercapacitor electrode.

EXPERIMENTAL METHODS

Materials and Deposition. Commercially available SnO₂ (<100 nm average, Sigma-Aldrich) and ZnO (100 nm, Sigma-Aldrich) powders were blended in a mass ratio of 2:1 using a high-energy ball mill (PL-BMSL, AC 220 V 50/60 Hz, Poong Lim Tech., Korea). Considering that the lower electrochemical potential of SnO₂ induces fast redox reactions, the ratio of SnO₂/ZnO was set at 2:1 to obtain SnO₂-rich Zn₂SnO₄. The mechanochemical processing of the powders with ceramic aluminosilicate balls for 72 h produced nanoparticles of Zn₂SnO₄/SnO₂. These nanoparticles of Zn₂SnO₄/SnO₂ (0.30 g) were then mixed with approximately 40 mL of *N,N*-dimethylformamide (DMF, Reagent Duksan, Korea). Next, 0.3 mL of polyacrylonitrile (PAN, M_w = 150 kDa, Sigma-Aldrich)/DMF solution was added to the Zn₂SnO₄/SnO₂/DMF mixture as a dispersant to support the

formation of a stable colloidal dispersion. CNT/Zn₂SnO₄/SnO₂ colloidal dispersions with different CNT concentrations were prepared by adding the appropriate amount of CNTs to the precursor dispersion and stirring until the CNTs were well dispersed (see Figure 1a). This precursor was then delivered to a cold spray system using a

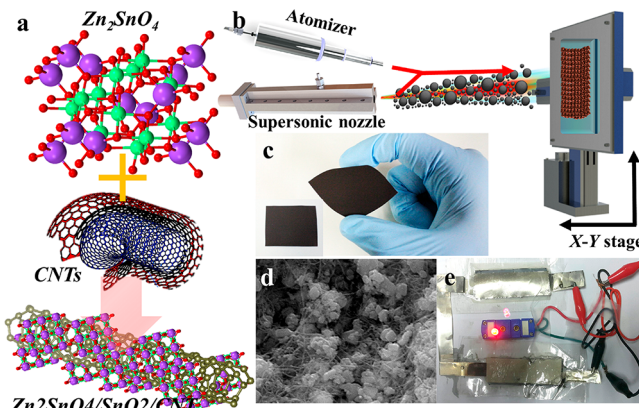


Figure 1. (a) Schematic structures of Zn₂SnO₄/SnO₂, CNT, and Zn₂SnO₄/SnO₂/CNT. (b) Schematic of the supersonic cold spray system. (c) Annealed sample deposited using cold spray. (d) SEM of Zn₂SnO₄/SnO₂/CNT blend. (e) Flexible supercapacitor-powered LED.

syringe pump (LEGATO 210, KD Scientific). The supersonic cold spray system operating in open-air conditions (a “nonvacuum coating method) was used for deposition; its schematic is shown in Figure 1b. Preheated air was injected into a de Laval nozzle at a pressure (4 bar) that accelerated the air and CNT/Zn₂SnO₄/SnO₂ colloidal dispersions to a supersonic velocity. The solvent evaporated, and the particles were deposited on nickel foil (8 × 8 cm²) at a supersonic speed (see Figure 1c). The nozzle dimensions and other process parameters are listed in Table 1. The substrate was mounted on an x-

Table 1. Process Parameters

experimental conditions	parameter values
propellant gas	air
gas pressure	4 bar
gas temperature	200 °C
nozzle to substrate distance	13 cm
x-y stage speed	1 cm s ⁻¹
precursor flow rate	1.5 mL min ⁻¹

y stage that was translated to produce a uniform deposition. The deposition of Zn₂SnO₄/SnO₂ and its composites was carried out for $N = 10$ passes. In addition, an undoped ZnO (without SnO₂) film was fabricated by spraying a ZnO/DMF dispersion.

The samples were finally annealed in Ar environment, in which the temperature was raised from room temperature to 500 °C at a rate of 3 °C min⁻¹. The temperature of 500 °C was maintained for 30 min, and then the film was allowed to cool naturally in the furnace. Figure 1d shows the intermingled CNT and Zn₂SnO₄/SnO₂. A symmetric supercapacitor assembled from a pair of Zn₂SnO₄/SnO₂/CNT flexible electrodes was used to power a red LED, as shown in Figure 1e.

Characterization. The morphology of the samples was analyzed using scanning electron microscopy (FESEM, S-5000, Hitachi, Ltd.), transmission electron microscopy (TEM, JEM 2100F, JEOL, Inc.), and energy-dispersive X-ray spectroscopy (EDS). For TEM, the samples were directly coated on Cu grids. Raman spectroscopy (Jasco, NRS-3100) was employed to analyze the CNT and other chemical bonds based on their vibrational response. The crystal structures of the Zn₂SnO₄/SnO₂ sample and Zn₂SnO₄/SnO₂/CNT composite sample were investigated using X-ray diffraction (XRD, SmartLab,

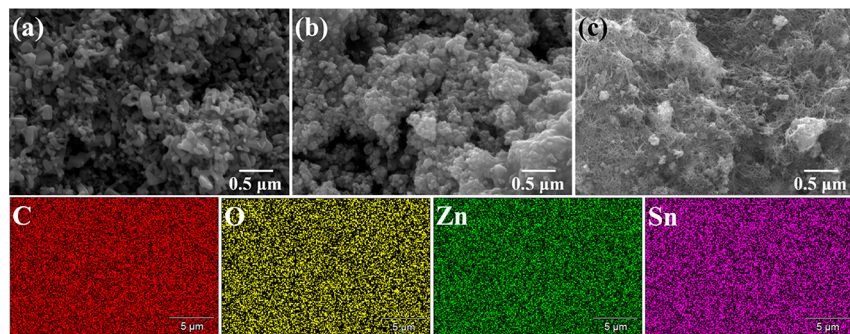


Figure 2. SEM images of (a) ZnO, (b) Zn₂SnO₄/SnO₂, and (c) Zn₂SnO₄/SnO₂/CNT and elemental mapping of C, O, Zn, and Sn obtained using EDS.

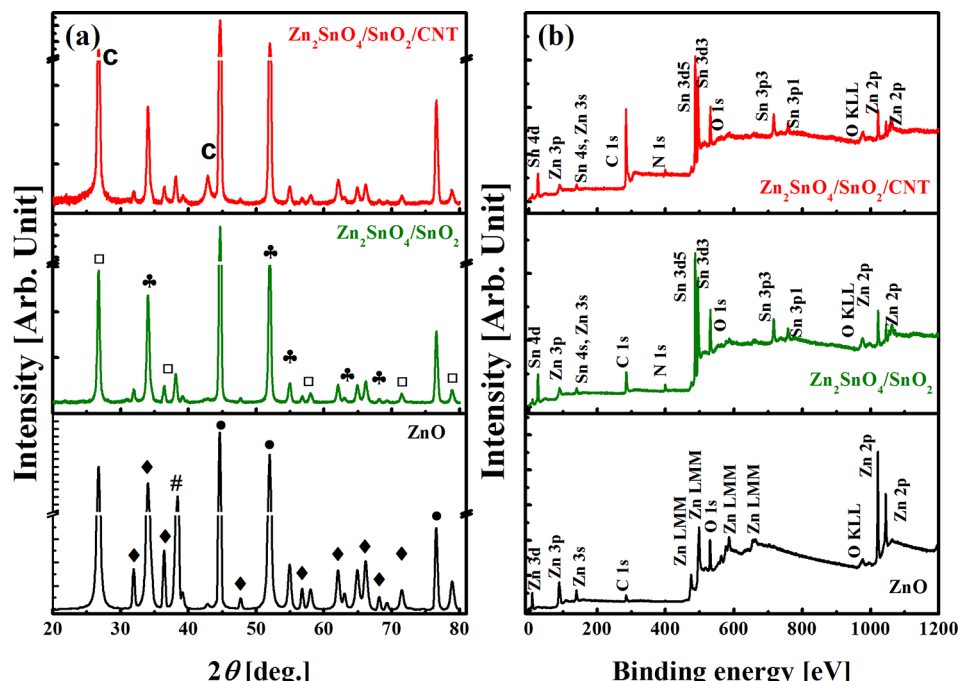


Figure 3. (a) XRD patterns and (b) XPS survey spectra of synthesized ZnO, Zn₂SnO₄/SnO₂, and Zn₂SnO₄/SnO₂/CNT materials.

Rigaku) over a 2θ range of 20–80°. The oxidation states of the elements present on the surface of the samples were determined using X-ray photoelectron spectroscopy (XPS, Theta Probe Base System, Thermo Fisher Scientific Co.). The sheet resistances of the samples were measured using a sheet resistance meter (FPP-400, Dasol ENG).

Electrochemical Measurements. Cyclic voltammetry (CV) and electrochemical impedance spectroscopy (EIS) measurements were performed using a potentiostat (VersaSTAT-3, Princeton Applied Research, USA). The Zn₂SnO₄/SnO₂/CNT composite electrode tests were conducted using two electrodes (symmetric supercapacitor). The EIS measurements were carried out over a frequency range from 100 kHz to 0.1 Hz with an amplitude of 10 mV. Symmetric coin cells (CR2032) were also used to conduct the galvanostatic charge–discharge (GCD) study using a WBCS3000 battery testing system (WonATech, Seoul, South Korea). The coin cells were prepared using two Zn₂SnO₄/SnO₂/CNT composite electrodes (14 mm in diameter) that were electrically isolated using a polymer separator (Celgard 3501; Celgard, Chungbuk, South Korea).

The electrochemical properties of Zn₂SnO₄/SnO₂/CNT electrodes were evaluated at a room temperature of 25 °C with a 6 M KOH aqueous electrolyte. Such aqueous electrolytes are less expensive than ionic liquids or organic electrolytes. The specific capacitance, energy density, and power density were calculated using the following equations. The specific capacitance values were calculated using the discharge time as follows³⁴

$$C_s = \frac{4I}{m(dV/dt)} \quad (1)$$

Here, C_s is the specific capacitance ($F \cdot g^{-1}$), I is the specific current (A), m is the combined mass of both electrodes (g), and dV/dt is calculated from the slope of the galvanostatic discharge curve. The energy and power density equations are as follows³⁵

$$E = \frac{1}{2} \cdot C_s \cdot \Delta V^2 \quad (2)$$

$$P = \frac{E}{\Delta t} \quad (3)$$

Here, E is the energy density, ΔV is the potential window, Δt is the discharge time, and P is the power density.

RESULTS AND DISCUSSION

Surface Morphology and Elemental Composition.

The surface morphologies of various samples are presented in the SEM images shown in Figure 2. The agglomerates of ZnO and Zn₂SnO₄/SnO₂ deposited on Ni foil are shown in Figure 2a and 2b, respectively. In the composite, well-dispersed CNTs (fiber-like structures) were observed within the agglomerates of Zn₂SnO₄/SnO₂ (Figure 2c). The intermingled CNTs

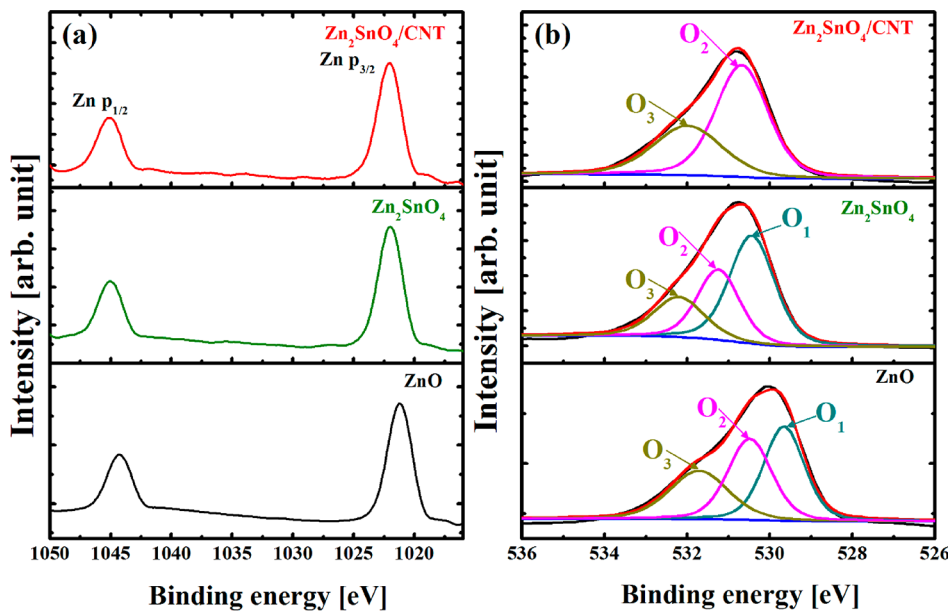


Figure 4. XPS high-resolution spectra of (a) Zn 2p and (b) O 1s regions for ZnO, Zn₂SnO₄/SnO₂, and Zn₂SnO₄/SnO₂/CNT samples.

reduce the agglomeration of Zn₂SnO₄/SnO₂ particles. In addition, the network of CNTs and Zn₂SnO₄/SnO₂ particles delivers a faster electron transfer when used as electrode in a SC. The uniform distributions of carbon (C), oxygen (O), zinc (Zn), and tin (Sn) in the composites are presented in the EDS elemental maps shown in Figure 2. The Raman spectrum in Figure S1 (Supporting Information) shows peaks at 1350, 1582, and 2670 cm⁻¹ corresponding to the defective D band, graphitic G band, and 2D band of the CNT, respectively. Comparing the peaks of Zn₂SnO₄/SnO₂/CNT at 1350 and 1582 cm⁻¹ with pristine CNT shown in Figure S1 (Supporting Information) shows that pristine CNTs are rich in graphitic phase. The I_D/I_G ratio of CNT powder was 0.31. The corresponding ratios (I_D/I_G) in ZnO and Zn₂SnO₄/SnO₂ cases were 1.57 and 1.59, respectively, reflecting the disordered carbon produced by annealing of PAN. However, in the case of Zn₂SnO₄/SnO₂/CNT, the carbon was more graphitic and less defective, with an I_D/I_G ratio of 1.04, significantly lower than that of ZnO and Zn₂SnO₄/SnO₂ but also much higher than that of the pristine CNTs. The I_D/I_G ratio greater than one in the composite results from the strong interaction between CNTs and Zn₂SnO₄/SnO₂ induced by the cold spray deposition of the composite films as well as the presence of defective carbon produced from PAN.

Crystal Structure and Surface Functional Group Analysis. The XRD patterns of ZnO, Zn₂SnO₄/SnO₂, and Zn₂SnO₄/SnO₂/CNT are shown in Figure 3a, where the diffraction peaks of Ni are observed at 2θ values of 44.4°, 52°, and 76° from (111), (200), and (220) planes, respectively, of the Ni substrate (circles, JCPDS 40-0850) along with a peak of NiO at 38° (pound signs, JCPDS 47-1049). The ZnO sample shows diffraction peaks at 34.4°, 36.2°, 47.5°, 56.6°, 62.8°, 66.4°, 67.9°, and 72.5° from (002), (101), (102), (110), (103), (200), (112), and (204) planes of ZnO, respectively (diamonds, JCPDS 36-1451). The bimetallic sample shows peaks corresponding to Zn₂SnO₄, confirming its formation by cold welding during ball milling. The diffraction peaks of Zn₂SnO₄ at 34.1°, 51.7°, 55.14°, 63.5°, and 68.6° correspond to (311), (422), (511), (440), and (620) planes, respectively

(clovers, JCPDS file no. 24-1470). The diffraction peaks of SnO₂ are observed at 2θ values of 26.6°, 37.9°, 57.9°, 71.4°, and 78.8° from (110), (200), (002), (202), and (321) planes, respectively (squares, JCPDS file no. 72-1147). The dominant diffraction peaks of the CNT are also observed at 26.6° and 42.8° (denoted by C in Figure 3a) corresponding to (002) and (100) planes, respectively.

The XPS survey spectra of ZnO, Zn₂SnO₄/SnO₂, and Zn₂SnO₄/SnO₂/CNT in Figure 3b show the surface chemical compositions. The XPS survey spectrum of ZnO shows Zn, O, and weak C and N signals. Further, along with Zn and O, Sn signals at 486.7 and 495.1 eV were obtained in Zn₂SnO₄/SnO₂ and composite sample. The core spectra of Sn are shown in Figure S2 (Supporting Information). The presence of C and N in ZnO and Zn₂SnO₄/SnO₂ was due to carbonization of PAN added as a dispersant to stabilize the nanoparticle colloids. The C peak became much stronger when CNTs were added to obtain Zn₂SnO₄/SnO₂/CNT composite.

The high-resolution XPS spectra in the Zn 2p and O 1s energy ranges for different samples are shown in Figure 4a and 4b, respectively. The Zn 2p core spectrum contained a doublet (Zn 2p_{3/2} and Zn 2p_{1/2}) with a slight variation in the peak positions due to the metal ions that formed Zn–O–Sn bonds in the bimetallic oxide. Thus, the electronic interactions of two different atoms resulted in chemical shifts in the binding energies. The binding energy difference of approximately 23 eV between the Zn 2p_{3/2} and the Zn 2p_{1/2} levels (close to the standard value of 22.97 eV) indicated the presence of Zn in the Zn²⁺ oxidation state. The oxygen O 1s core spectra for all samples were fitted to three Gaussian peaks, labeled as O₁, O₂, and O₃, in Figure 4b. The O₁ peak with lower binding energy in the O 1s spectrum corresponds to O²⁻ ions bonded to Zn²⁺/Sn²⁺ ions. The oxygen-deficient regions within the metal oxide lattice gave rise to the O₂ peak at 530.7 eV. The varying intensity of the O₂ peak reflected the variations in the concentration of O vacancies. The surface-adsorbed O, in compounds such as CO₂ and H₂O, gave rise to the O₃ peak at higher binding energies. Further, the differences in the peak positions of Zn 2p and O 1s for each sample are listed in Table

Table 2. XPS Analysis Showing the Peak Positions of the Elements Present

sample	binding energy of O _{1s} , O ₂ , and O ₃ deconvoluted peaks of oxygen O 1s (eV)			binding energy of Zn 2p doublet and its difference (Δ) (eV)		
	O ₁	O ₂	O ₃	Zn 2p _{3/2}	Zn 2p _{1/2}	Δ (eV)
ZnO	529.54	530.50	531.07	1021.22	1044.30	23.08
Zn ₂ SnO ₄	530.40	531.15	532.21	1021.99	1045.06	23.07
Zn ₂ SnO ₄ /CNT		530.60	532.09	1022.07	1045.12	23.05

2. The high-resolution spectra in the C 1s and N 1s ranges are shown in Figure S3 (Supporting Information). The C 1s spectrum can be deconvoluted into peaks at 284, 284.6, 285.7, 287.5, and 288.8 eV, which are attributed to C=C sp², C-C sp³, C-OH, C-O, and C=O, respectively. The C=C sp² and C-C sp³ in Zn₂SnO₄/SnO₂/CNT sample support the presence of CNT, whereas C-C sp³ in ZnO and Zn₂SnO₄/SnO₂ is due to the presence of adventitious carbon.

The morphological characteristics of the Zn₂SnO₄/SnO₂/CNT composite were further substantiated by TEM imaging, as shown in Figure 5a. The TEM image shows particles of

des at a scan rate of 100 mV·s⁻¹. During the positive linear voltage sweep, the anodic (positive) curve corresponded to oxidation of the electrode. The CV capacitive curves reversed during discharge, and the cathodic current reached a peak value owing to the fast and efficient reversible electrode reaction. The ZnO electrode showed a gradual decrease of the current, whereas the other two electrodes (Zn₂SnO₄/SnO₂ and Zn₂SnO₄/SnO₂/CNT) showed almost capacitive characteristics. For the Zn₂SnO₄/SnO₂ electrode, the bimetallic oxide facilitated ionic transport and enhanced the redox reaction reversibility owing to multielectron availability. Furthermore, Zn₂SnO₄/SnO₂/CNT delivered both EDLC and pseudocapacitance, and hence, a broader CV curve was obtained compared to the Zn₂SnO₄/SnO₂ electrodes. The quasi-rectangular shape of Zn₂SnO₄/SnO₂/CNT electrodes (see Figure 6a) indicates improved capacitive features. The concentration of CNT was optimized, and CV was evaluated for each electrode at different scan rates, as shown in Figure S4 (Supporting Information). Increasing the CNT concentration resulted in CV curves with dominant EDLC characteristics (see Figure S4, Supporting Information). Zn₂SnO₄/SnO₂/CNT composites exhibited better conductivity, larger surface area, and higher current response than those without CNT. Thus, from the CV analysis, Zn₂SnO₄/SnO₂/CNT_{100mg} provided the optimal current response to the applied potential. We also performed cyclic voltammetry measurements for SnO₂ samples at various scan rates, as shown in Figure S5a (Supporting Information). Furthermore, the relationship between the square root of scan rate and the anodic/cathodic peak current was observed to be linear (see Figure S5b, Supporting Information). Unlike ZnO CV curves, SnO₂ samples show more horizontal anodic and cathodic curves (see Figure 6a). The diagonal-type CV curves of ZnO could be due to higher resistance and lower electron mobility. Furthermore, potential window is a critical parameter for pseudocapacitors operating with aqueous electrolytes to lower the cost of the SC electrodes. To address this issue, the CV curves for Zn₂SnO₄/SnO₂/CNT_{100mg} were measured over several potential windows, as shown in Figure 6b. A narrow potential window lowers the energy density in accordance with eq 2. The CV curve for Zn₂SnO₄/SnO₂/CNT_{100mg} in the broader potential window (0–1.2 V) did not show irreversible reactions or battery-like redox peaks. Thus, this wider potential window could be used to enhance the energy density. The anodic and cathodic peak currents increased linearly with the square root of the scan rate (see Figure 6c), confirming the capacitive and reversible characteristics of the SC electrodes.³⁵ Moreover, the linear relationship between the peak current and the square root of the scan rate suggests a diffusion-controlled energy storage process. The faster electrolytic ion diffusion in the active material (Zn₂SnO₄/SnO₂/CNT) also contributes to the enhanced electrochemical activity.^{35–37}

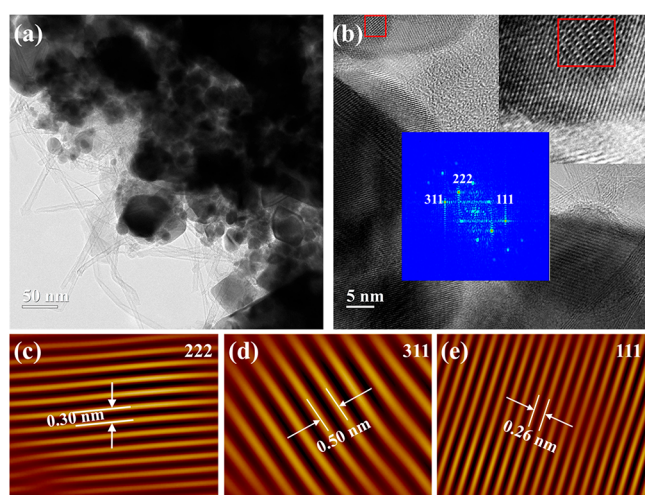


Figure 5. (a) TEM images of Zn₂SnO₄/SnO₂/CNT composite. (b) HRTEM (upper right inset), fast Fourier transformation (FFT, lower inset), and inverse FFT for the (c) 222, (d) 311, and (e) 111 planes of Zn₂SnO₄.

Zn₂SnO₄/SnO₂ intermingled with tube-like structures of CNT. The high-resolution transmission electron microscopy (HRTEM) of the sample also provided crystallographic information. The selected area (left red square) of the HRTEM shown in Figure 5b was magnified and is shown as the upper inset image. The red square (right side) was selected to obtain the FFT (lower inset of Figure 5b). The FFT image shows diffraction spots that corresponded to (222), (311), and (111) planes of crystalline Zn₂SnO₄. The inverse FFT of three diffraction spots shows lattice fringes with *d*-spacing values of 0.30, 0.50, and 0.26 nm corresponding to (222), (311), and (111) planes, respectively. The interplanar distances shown in Figures 5c–e correspond to Zn₂SnO₄.

Electrochemical Analysis. In electrochemistry, CV curves display current as a function of the applied voltage. CV is widely used to observe the electrochemical response of energy storage devices, study their degradation processes, and determine the capacitive potential window of SC electrodes. Figure 6a shows the current responses to the applied voltages for ZnO, Zn₂SnO₄/SnO₂, and Zn₂SnO₄/SnO₂/CNT electrodes.

Furthermore, electrochemical impedance spectroscopy provided insight into significant characteristics of the super-

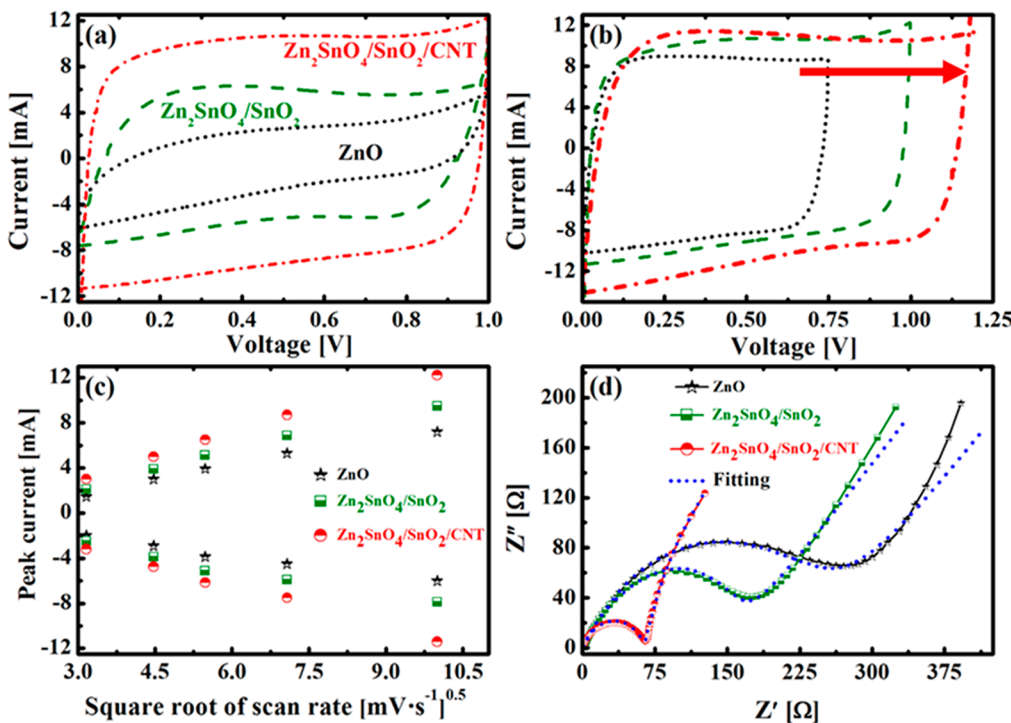


Figure 6. CV measurements of (a) ZnO, Zn₂SnO₄/SnO₂, and Zn₂SnO₄/SnO₂/CNT at a scan rate of 100 mV·s⁻¹. (b) CV curves of Zn₂SnO₄/SnO₂/CNT over different potential windows. (c) Peak current as a function of the square root of the scan rate. (d) Nyquist plots of EIS data for the three samples.

capacitor electrodes. The plots displayed a semicircle in the high-frequency region under a low alternating voltage amplitude (10 mV) and an inclined linear response at a lower frequency, corresponding to the electrolyte ion diffusion and EDL formation, as shown in Figure 6d. The Nyquist diagram (Figure 6d) is a well-known impedance plot that represents the imaginary impedance (Z'') as a function of the real impedance (Z'). The x -axis initial intercept of the semicircle indicates the electrolyte resistance (R_s), and the diameter of the semicircle arc indicates the charge-transfer resistance (R_{ct}) of the electrode. The EIS data were fitted to an equivalent circuit model (see inset of Figure S6, Supporting Information), and the values of R_s , R_{ct} internal resistance (IR), constant phase element (CPE), and capacitance (C) from the fitting process of each electrode are listed in Table 3. The small

resistances of ZnO and Zn₂SnO₄ were 7.3 and 6.8 mΩ/sq, respectively, and the resistance varied from 3.7 to 2.1 mΩ/sq with increasing CNT concentration, as shown in Table S1 (Supporting Information). The fitting parameters listed in Table 3 revealed that increasing the CNT concentration reduced the charge-transfer resistance, which was consistent with the fast electron transport provided by CNTs, as shown in Figure 6d. The EIS results were consistent with the electrochemical response demonstrated by the CV curves shown in Figure 6a and Figure S4 (Supporting Information).

The GCD measurements reconfirmed the capacitive characteristics of the composite samples. Measurements on the different samples were conducted over a voltage range of 0–1 V at current densities of 1–10 A·g⁻¹ for ZnO, Zn₂SnO₄/SnO₂, and Zn₂SnO₄/SnO₂/CNT (with different CNT concentrations), and the corresponding results are as shown in Figure S7 (Supporting Information). A comparison of the GCD curves of ZnO, Zn₂SnO₄/SnO₂, and Zn₂SnO₄/SnO₂/CNT at a specific current density of 1 A·g⁻¹ is shown in Figure 7a. ZnO did not produce triangular charge–discharge curves characteristic of the capacitive behavior. The sudden decrease in the potential during the discharge of ZnO samples could be because of their high internal resistance (see Table 3), as also observed in the EIS results (Figure 6d). Zn₂SnO₄/SnO₂ and Zn₂SnO₄/SnO₂/CNT electrodes displayed pseudocapacitive behavior that was closer to the triangular charge–discharge curve characteristics of the EDLC behavior (see Figure 7a). However, the bimetallic oxide (Zn₂SnO₄/SnO₂) electrode without CNTs had a shorter charge/discharge duration owing to its slower electron transfer rate (see Figure 6d). The optimal composition of Zn₂SnO₄/SnO₂/CNT showed the synergistic effects of faster charge transfer and larger energy storage capacity. A detailed study of GCD curves (see Figure S7, Supporting Information) for different samples at various

Table 3. Parameters Obtained by Fitting of the Nyquist Plot Using the Randle Equivalent Circuit

samples	R_s [Ω]	R_{ct} [Ω]	IR [Ω]	CPE [S·sec ⁿ]	C [F]
ZnO	2.58	255.0	257.6	6.78e-5	7.811e-5
ZSO	2.53	158.9	161.4	0.0037	1.091e-5
ZTC50	1.46	114.8	116.3	0.0019	2.022e-5
ZTC75	1.38	59.6	61.0	0.0056	3.322e-6
ZTC100	0.86	57.0	57.9	0.0113	2.003e-6
ZTC125	0.81	42.9	43.7	0.0104	2.003e-6

electrolyte solution resistance (R_s) indicated excellent electron and electrolytic ion transport, provided by the large electrochemically active surface area and the coarse morphology of the nanocomposite electrodes. The decrease in resistance due to the incorporation of CNT, as exhibited by the impedance spectroscopy, was consistent with the measured electrical resistance obtained using a sheet resistance meter. The

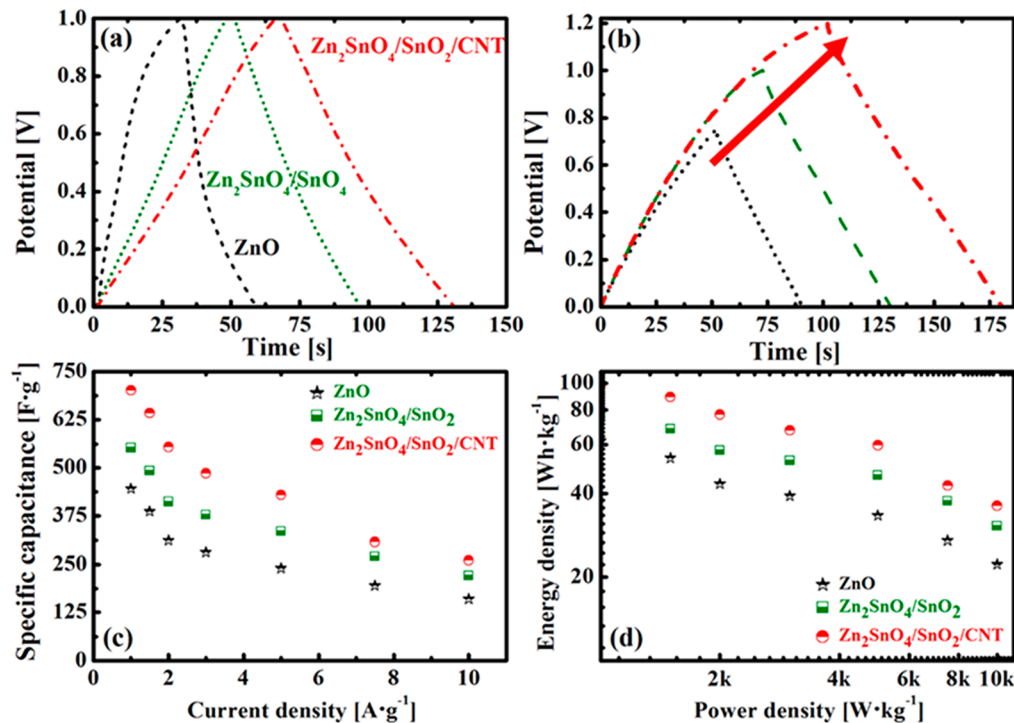


Figure 7. GCD curve comparison for (a) different samples and (b) different potential windows (for Zn₂SnO₄/SnO₂/CNT) at a specific current density of 10 A·g⁻¹. (c) Specific capacitance and (d) energy density of ZnO, Zn₂SnO₄/SnO₂, and Zn₂SnO₄/SnO₂/CNT samples for current densities ranging from 1 to 10 A·g⁻¹.

Table 4. Comparison of the Specific Capacitances of Electrodes of Similar Materials to the Composites Synthesized in This Study

materials	capacitance[F·g ⁻¹]/electrolyte	current density [A·g ⁻¹]	potential window [V]	retention[%]/no. of cycles	ref
MnO ₂ /ZnO	251/1 M KOH	0.5		100/5000	38
CoNi-CoNiO ₂ -CMK-3	280/6 M KOH	0.25	0 to -1	98/10000	39
ZnO/rGO	277/6 M KOH	0.05	0 to 1	97/15000	40
ZnO/AC	155	0.5	0 to -1	73/1000	41
ZnSb ₂ O ₆	9/1 M H ₂ SO ₄	1	0 to 0.65	100/500	42
Zn-SnO ₂	132/2 M KOH	1	0 to 0.5	92/500	43
ZnCo ₂ O ₄	647/2 M KOH	1	0 to 0.5	92/2000	44
ZnCo ₂ O ₄	776/2 M KOH	1	0 to 0.45	84/1500	45
Zn ₂ SnO ₄ /MnO ₂ /CMF	642/1 M Na ₂ SO ₄	1	0 to 0.8	98.8/1000	46
Zn ₂ SnO ₄	323/6 M KOH	1	0 to 0.5	97/3000	47
Zn ₂ SnO ₄ /SnO ₂ /CNT	702/6 M KOH	1	0 to 1	93/15000	present

current densities was carried out to optimize the CNT composition in the bimetallic oxide. Results in Figure S7 (*Supporting Information*) show that CNT-based electrodes charge and discharge rapidly with an increase in the current density, thereby exhibiting the ideal characteristics of capacitors. Figure 7b shows GCD measurement curves for Zn₂SnO₄/SnO₂/CNT over different potential windows. The charge/discharge time was observed to increase linearly with increase in potential window, as shown in Figure 7b. Use of a wider potential window allows more charge storage, thereby resulting in higher capacitance and energy density. The aqueous electrolyte has a limitation of 1.23 V, which is the minimum potential for splitting water. If the biasing voltage is increased beyond this value there is a possibility of water oxidation. Therefore, the measurements in this study were restricted to 1.2 V.

Figure 7c shows that the specific capacitances of ZnO, Zn₂SnO₄/SnO₂, and Zn₂SnO₄/SnO₂/CNT electrodes reached

446, 552, and 702 F·g⁻¹ at a current density of 1 A·g⁻¹ and decreased to 160, 220, and 260 F·g⁻¹ at a high current density of 10 A·g⁻¹, respectively. The Zn₂SnO₄/SnO₂/CNT and Zn₂SnO₄/SnO₂ demonstrated similar current rate retention of 37% and 39%, respectively, upon increasing the current density from 1 to 10 A·g⁻¹. The embedding of CNT within Zn₂SnO₄/SnO₂ may limit the ability of CNT to enhance the current rate capability of Zn₂SnO₄/SnO₂/CNT. At a higher current rate, the electrolytic ions do not diffuse deep enough to reach all of the available CNT. However, the CNT underneath Zn₂SnO₄/SnO₂ provides faster electron transfer, significantly improves long-term stability, and exhibits higher capacitance at a lower current rate (see Figure 7c). Moreover, the composite of CNTs and Zn₂SnO₄/SnO₂ and the grafting of Zn₂SnO₄/SnO₂ particles on the CNTs can accommodate more charges and improve the electrochemical performance. The electrochemical performance of rarely reported Zn₂SnO₄/SnO₂ along with several other Zn-based bimetallic oxides is listed in Table 4 for

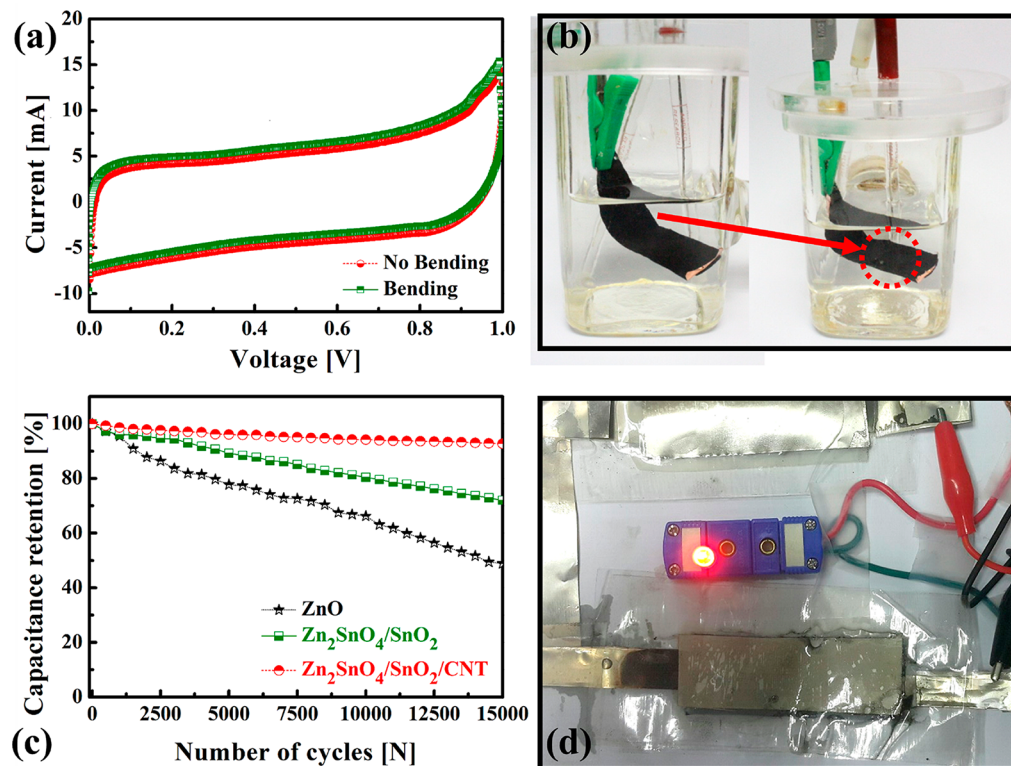


Figure 8. (a) CV measurements Zn₂SnO₄/SnO₂/CNT electrodes with and without bending. (b) Cyclic voltammetry measurement on a bent supercapacitor electrode. (c) Capacitance retention during long-term cycling measurements of ZnO, Zn₂SnO₄/SnO₂, and Zn₂SnO₄/SnO₂/CNT. (d) LED powered using two symmetric supercapacitors.

comparison with the present work. The energy density was also evaluated using the specific capacitance of the SC electrodes. The Ragone plot (see Figure 7d) shows energy density as a function of power density (1000–10 000 W·kg⁻¹). A high energy density of approximately 98 Wh·kg⁻¹ was achieved for the composite electrode at a power density of 1000 W·kg⁻¹. The energy density of ZnO was approximately 62 Wh·kg⁻¹, while Zn₂SnO₄/SnO₂ exhibited an energy density of approximately 77 Wh·kg⁻¹ at the same power density. The Zn₂SnO₄/SnO₂/CNT composite electrode exhibited an energy density of 36 Wh·kg⁻¹ at a higher power density of 10 000 W·kg⁻¹.

The results of this study, compared to those obtained using other bimetallic oxides and their composites, showed a higher capacitance and better electrochemical stability owing to the combination of CNT and Zn₂SnO₄. The enhanced electrochemical performance of Zn₂SnO₄/SnO₂/CNT electrodes compared to ZnO and Zn₂SnO₄/SnO₂ SC electrodes could be because of the EDLC provided by the CNT anchoring Zn₂SnO₄/SnO₂ particles without agglomeration. The composite was able to adsorb K⁺ ions on the surface and allow intercalation/deintercalation of K⁺ ions in the intermingled CNTs and Zn₂SnO₄/SnO₂. Figure S8 (Supporting Information) shows an SEM image, oxide particle/composite adsorbing the ions, and corresponding voltammograms, suggesting that the EDL formation plays an important role for Zn₂SnO₄/SnO₂/CNT electrodes, whose voltammogram was more rectangular in shape than that of two electrodes without CNTs.

The quasi-rectangular CV curves indicating the capacitive characteristics of the Zn₂SnO₄/SnO₂/CNT electrode remained unchanged during bending tests, as shown in Figure 8a. The

change in the current response was negligible as shown by the CV curves for Zn₂SnO₄/SnO₂/CNT with (for first bending test) and without bending. However, the current response after 100 bending cycles was reduced slightly, and the cyclic voltammetry curve became narrower as shown in Figure 8a. The CV measurement setup using the bent Zn₂SnO₄/SnO₂/CNT electrode is shown in Figure 8b. The long-term cycling performance is an important parameter for assessing the performance of supercapacitors and electrodes. Therefore, the long-term GCD measurements for ZnO, Zn₂SnO₄/SnO₂, and Zn₂SnO₄/SnO₂/CNT were carried out, and the corresponding specific capacitance (considering discharge only) retentions after 15 000 cycles at a current density of 10 A·g⁻¹ are shown in Figure 8c. The specific capacitance retentions of ZnO, Zn₂SnO₄/SnO₂, and Zn₂SnO₄/SnO₂/CNT were 49%, 72%, and 93% after 15 000 cycles (see Figure 8c), respectively. The higher long-term cycling stability of Zn₂SnO₄/SnO₂/CNT compared to the other two electrodes was due to the lower charge-transfer resistance of the intermingled CNT and Zn₂SnO₄/SnO₂ active material (see Figure 6d). The presence of CNT overcame the poor conductivity issue of Zn₂SnO₄/SnO₂ and provided faster charge transport along with inhibiting agglomeration of Zn₂SnO₄/SnO₂ particles, resulting in an improved electrochemical performance and stability. Table 4 compares the excellent capacitance retention of Zn₂SnO₄/SnO₂/CNT to the values reported previously for SCs based on similar materials. As a visual demonstration, two symmetric supercapacitors (1.0 by 3.5 cm electrodes) were used to power a red LED, as shown in Figure 8d.

CONCLUSIONS

Electrodes produced using a mixed multivalent metal oxide (Zn_2SnO_4/SnO_2) and carbon nanotubes (CNTs) exhibited excellent pseudocapacitive characteristics. The CNTs contributed to the electrode's superior conductivity and enhanced double-layer capacitance. Electrochemical measurements demonstrated a high specific capacitance of $702 \text{ F}\cdot\text{g}^{-1}$ at a specific current of $1 \text{ A}\cdot\text{g}^{-1}$ for these nanocomposite electrodes. The optimized $Zn_2SnO_4/SnO_2/CNT$ electrode demonstrated a maximum energy density of approximately $98 \text{ Wh}\cdot\text{kg}^{-1}$ at a power density of $1000 \text{ W}\cdot\text{kg}^{-1}$ and displayed excellent cycling stability (93% capacity retention) over 15 000 GCD cycles. The demonstrated specific capacitance, energy density, and stable electrochemical performance make $Zn_2SnO_4/SnO_2/CNT$ a promising SC electrode material.

ASSOCIATED CONTENT

Supporting Information

The Supporting Information is available free of charge on the ACS Publications website at DOI: [10.1021/acssuschemeng.9b02549](https://doi.org/10.1021/acssuschemeng.9b02549).

Raman spectra of CNT, ZnO , Zn_2SnO_4/SnO_2 , and $Zn_2SnO_4/SnO_2/CNT$ composite; XPS high-resolution spectra of Sn in Zn_2SnO_4/SnO_2 and $Zn_2SnO_4/SnO_2/CNT$ samples; XPS high-resolution spectra of C 1s and N 1s for ZnO , Zn_2SnO_4/SnO_2 , and $Zn_2SnO_4/SnO_2/CNT$ samples; cyclic voltammetry curves for the various samples at different scan rates; cyclic voltammetry curves for SnO_2 samples at different scan rates, and peak current as a function of the square root of the scan rate for ZnO , SnO_2 , and Zn_2SnO_4/SnO_2 ; Nyquist plot of $Zn_2SnO_4/SnO_2/CNT_{50\text{mg}}$, $Zn_2SnO_4/SnO_2/CNT_{75\text{mg}}$, and $Zn_2SnO_4/SnO_2/CNT_{125\text{mg}}$ with the equivalent circuit employed for fitting the Nyquist data; electrical sheet resistance of different electrodes; galvanostatic charge–discharge curves for the various samples at different specific current densities; electrolyte interaction and energy storage mechanism representation and consequent capacitive characteristics of ZnO , Zn_2SnO_4/SnO_2 , and $Zn_2SnO_4/SnO_2/CNT$ (PDF)

AUTHOR INFORMATION

Corresponding Author

*E-mail: skyoon@korea.ac.kr.

ORCID

Edmund Samuel: [0000-0002-3916-3507](https://orcid.org/0000-0002-3916-3507)

Mark T. Swihart: [0000-0002-9652-687X](https://orcid.org/0000-0002-9652-687X)

Sam S. Yoon: [0000-0002-9031-4198](https://orcid.org/0000-0002-9031-4198)

Author Contributions

‡E.S. and T.-G.K.: These authors contributed equally.

Notes

The authors declare no competing financial interest.

ACKNOWLEDGMENTS

This research was supported by the Technology Development Program to Solve Climate Changes of the National Research Foundation (NRF) funded by the Ministry of Science, ICT & Future Planning (NRF-2016M1A2A2936760), NRF-2017R1A2B4005639, and NRF-2013R1A5A1073861.

REFERENCES

- (1) Cakici, M.; Kakarla, R. R.; Alonso-Marroquin, F. Advanced electrochemical energy storage supercapacitors based on the flexible carbon fiber fabric-coated with uniform coral-like MnO_2 structured electrodes. *Chem. Eng. J.* **2017**, *309*, 151–158.
- (2) Rojas-Cessa, R.; Grebel, H.; Jiang, Z.; Fukuda, C.; Pita, H.; Chowdhury, T. S.; Dong, Z.; Wan, Y. Integration of alternative energy sources into digital micro-grids. *Environ. Prog. Sustainable Energy* **2018**, *37* (1), 155–164.
- (3) Xiong, D.; Li, X.; Bai, Z.; Lu, S. Recent Advances in Layered $Ti_3C_2T_x$ MXene for Electrochemical Energy Storage. *Small* **2018**, *14* (17), 1703419.
- (4) Dai, K.; Wang, X.; Yin, Y.; Hao, C.; You, Z. Voltage fluctuation in a supercapacitor during a high-g impact. *Sci. Rep.* **2016**, *6*, 38794.
- (5) Thangavel, R.; Kannan, A. G.; Ponraj, R.; Thangavel, V.; Kim, D.-W.; Lee, Y.-S. High-energy green supercapacitor driven by ionic liquid electrolytes as an ultra-high stable next-generation energy storage device. *J. Power Sources* **2018**, *383*, 102–109.
- (6) Chen, B.; Jiang, Y.; Tang, X.; Pan, Y.; Hu, S. Fully packaged carbon nanotube supercapacitors by direct ink writing on flexible substrates. *ACS Appl. Mater. Interfaces* **2017**, *9* (34), 28433–28440.
- (7) Zuliani, J. E.; Jia, C. Q.; Kirk, D. W. Elucidating the Importance of Pore Structure in Determining the Double-Layer Capacitance of Nanoporous Carbon Materials. *J. Phys. Chem. C* **2017**, *121* (38), 20555–20566.
- (8) Rabbow, T. J.; Whitehead, A. H. Deconvolution of electrochemical double layer capacitance between fractions of active and total surface area of graphite felts. *Carbon* **2017**, *111*, 782–788.
- (9) Zhai, T.; Sun, S.; Liu, X.; Liang, C.; Wang, G.; Xia, H. Achieving Insertion-Like Capacity at Ultrahigh Rate via Tunable Surface Pseudocapacitance. *Adv. Mater.* **2018**, *30* (12), 1706640.
- (10) Lee, J.-S. M.; Briggs, M. E.; Hu, C.-C.; Cooper, A. I. Controlling electric double-layer capacitance and pseudocapacitance in heteroatom-doped carbons derived from hypercrosslinked microporous polymers. *Nano Energy* **2018**, *46*, 277–289.
- (11) Monguzzi, A.; Oertel, A.; Braga, D.; Riedinger, A.; Kim, D. K.; Knüsel, P. N.; Bianchi, A.; Mauri, M.; Simonutti, R.; Norris, D. J. Photocatalytic Water-Splitting Enhancement by Sub-Bandgap Photon Harvesting. *ACS Appl. Mater. Interfaces* **2017**, *9* (46), 40180–40186.
- (12) Zhang, Y.; Chen, H.; Guan, C.; Wu, Y.; Yang, C.; Shen, Z.; Zou, Q. Energy-saving Synthesis of MOF-Derived Hierarchical and hollow $Co(VO_3)_2\text{-}Co(OH)_2$ Composite Leaf Arrays for Supercapacitor electrode materials. *ACS Appl. Mater. Interfaces* **2018**, *10*, 18440–18444.
- (13) Chang, Y.; Zhou, W.; Wu, J.; Ye, G.; Zhou, Q.; Li, D.; Zhu, D.; Li, T.; Nie, G.; Du, Y. High-performance flexible-film supercapacitors of layered hydrous $RuO_2/\text{poly}(3,4\text{-ethylenedioxothiophene})\text{-poly(styrenesulfonate)}$ through vacuum filtration. *Electrochim. Acta* **2018**, *283*, 744–754.
- (14) Samuel, E.; Jo, H. S.; Joshi, B.; Park, H. G.; Kim, Y. I.; An, S.; Swihart, M. T.; Yun, J. M.; Kim, K. H.; Yoon, S. S. High-performance supercapacitors using flexible and freestanding $MnO_x/\text{carbamide carbon nanofibers}$. *Appl. Surf. Sci.* **2017**, *423*, 210–218.
- (15) Samuel, E.; Joshi, B.; Jo, H. S.; Kim, Y. I.; An, S.; Swihart, M. T.; Yun, J. M.; Kim, K. H.; Yoon, S. S. Carbon nanofibers decorated with $FeOx$ nanoparticles as a flexible electrode material for symmetric supercapacitors. *Chem. Eng. J.* **2017**, *328*, 776–784.
- (16) Guan, B. Y.; Kushima, A.; Yu, L.; Li, S.; Li, J.; Lou, X. W. Coordination Polymers Derived General Synthesis of Multishelled Mixed Metal-Oxide Particles for Hybrid Supercapacitors. *Adv. Mater.* **2017**, *29* (17), 1605902.
- (17) Zhang, G.; Xiao, X.; Li, B.; Gu, P.; Xue, H.; Pang, H. Transition metal oxides with one-dimensional/one-dimensional-analogue nanostructures for advanced supercapacitors. *J. Mater. Chem. A* **2017**, *5* (18), 8155–8186.
- (18) Prasanna, K.; Santhoshkumar, P.; Jo, Y. N.; Sivagami, I. N.; Kang, S. H.; Joe, Y. C.; Lee, C. W. Highly porous CeO_2 nanostructures prepared via combustion synthesis for supercapacitor applications. *Appl. Surf. Sci.* **2018**, *449*, 454–460.

- (19) Liu, M.; Jain, A.; Rong, Z.; Qu, X.; Canepa, P.; Malik, R.; Ceder, G.; Persson, K. A. Evaluation of sulfur spinel compounds for multivalent battery cathode applications. *Energy Environ. Sci.* **2016**, *9* (10), 3201–3209.
- (20) Song, X.; Li, X.; Bai, Z.; Yan, B.; Xiong, D.; Lin, L.; Zhao, H.; Li, D.; Shao, Y. Rationally-designed configuration of directly-coated Ni₃S₂/Ni electrode by RGO providing superior sodium storage. *Carbon* **2018**, *133*, 14–22.
- (21) Liu, X.; Hao, Y.; Shu, J.; Sari, H. M. K.; Lin, L.; Kou, H.; Li, J.; Liu, W.; Yan, B.; Li, D.; Zhang, J.; Li, X. Nitrogen/sulfur dual-doping of reduced graphene oxide harvesting hollow ZnSnS₃ nano-microcubes with superior sodium storage. *Nano Energy* **2019**, *57*, 414–423.
- (22) Lee, D. G.; Kim, Y. A.; Kim, B.-H. Capacitive properties of hierarchically structured carbon nanofiber/graphene/MnO₂ hybrid electrode with nitrogen and oxygen heteroatoms. *Carbon* **2016**, *107*, 783–791.
- (23) Xu, S.; Fu, D.; Song, K.; Wang, L.; Yang, Z.; Yang, W.; Hou, H. One-dimensional WO₃/BiVO₄ heterojunction photoanodes for efficient photoelectrochemical water splitting. *Chem. Eng. J.* **2018**, *349*, 368–375.
- (24) Shi, Z.; Xing, L.; Liu, Y.; Gao, Y.; Liu, J. A porous biomass-based sandwich-structured Co₃O₄@ Carbon Fiber@ Co₃O₄ composite for high-performance supercapacitors. *Carbon* **2018**, *129*, 819–825.
- (25) Li, X.; Zhang, L.; He, G. Fe₃O₄ doped double-shelled hollow carbon spheres with hierarchical pore network for durable high-performance supercapacitor. *Carbon* **2016**, *99*, 514–522.
- (26) Zheng, S.; Xue, H.; Pang, H. Supercapacitors based on metal coordination materials. *Coord. Chem. Rev.* **2018**, *373*, 2–21.
- (27) Liu, J.; Chen, Z.; Chen, S.; Zhang, B.; Wang, J.; Wang, H.; Tian, B.; Chen, M.; Fan, X.; Huang, Y. Electron/Ion Sponge"-Like V-Based Polyoxometalate: Toward High-Performance Cathode for Rechargeable Sodium Ion Batteries. *ACS Nano* **2017**, *11* (7), 6911–6920.
- (28) Zhang, L.; Zheng, S.; Wang, L.; Tang, H.; Xue, H.; Wang, G.; Pang, H. Fabrication of metal molybdate micro/nanomaterials for electrochemical energy storage. *Small* **2017**, *13* (33), 1700917.
- (29) Sharma, G.; Naushad, M.; Kumar, A.; Devi, S.; Khan, M. R. Lanthanum/Cadmium/Polyaniline bimetallic nanocomposite for the photodegradation of organic pollutant. *Iran. Polym. J.* **2015**, *24* (12), 1003–1013.
- (30) Islam, M.; Ali, G.; Jeong, M.-G.; Choi, W.; Chung, K. Y.; Jung, H.-G. Study on the electrochemical reaction mechanism of NiFe₂O₄ as a high-performance anode for Li-ion batteries. *ACS Appl. Mater. Interfaces* **2017**, *9* (17), 14833–14843.
- (31) Li, X.; Wang, C. Significantly increased cycling performance of novel "self-matrix" NiSnO₃ anode in lithium ion battery application. *RSC Adv.* **2012**, *2* (15), 6150–6154.
- (32) Wu, Z.; Zhu, Y.; Ji, X. NiCo₂O₄-based materials for electrochemical supercapacitors. *J. Mater. Chem. A* **2014**, *2* (36), 14759–14772.
- (33) Lee, J.-G.; Joshi, B. N.; Lee, J.-H.; Kim, T.-G.; Kim, D.-Y.; Al-Deyab, S. S.; Seong, I. W.; Swihart, M. T.; Yoon, W. Y.; Yoon, S. S. Stable high-capacity lithium ion battery anodes produced by supersonic spray deposition of hematite nanoparticles and self-healing reduced graphene oxide. *Electrochim. Acta* **2017**, *228*, 604–610.
- (34) Stoller, M. D.; Ruoff, R. S. Best practice methods for determining an electrode material's performance for ultracapacitors. *Energy Environ. Sci.* **2010**, *3* (9), 1294–1301.
- (35) Joshi, B.; Park, S.; Samuel, E.; Jo, H. S.; An, S.; Kim, M.-W.; Swihart, M. T.; Yun, J. M.; Kim, K. H.; Yoon, S. S. Zeolitic imidazolate framework-7 textile-derived nanocomposite fibers as freestanding supercapacitor electrodes. *J. Electroanal. Chem.* **2018**, *810*, 239–247.
- (36) Mei, B.-A.; Li, B.; Lin, J.; Pilon, L. Multidimensional cyclic voltammetry simulations of pseudocapacitive electrodes with a conducting nanorod scaffold. *J. Electrochem. Soc.* **2017**, *164* (13), A3237–A3252.
- (37) Wang, L.; Duan, G.; Zhu, J.; Chen, S.-M.; Liu, X.-h.; Palanisamy, S. Mesoporous transition metal oxides quasi-nanospheres with enhanced electrochemical properties for supercapacitor applications. *J. Colloid Interface Sci.* **2016**, *483*, 73–83.
- (38) Prasankumar, T.; Irthaza Aazem, V.S.; Raghavan, P.; Prem Ananth, K.; Biradar, S.; Ilangoval, R.; Jose, S. Microwave assisted synthesis of 3D network of Mn/Zn bimetallic oxide-high performance electrodes for supercapacitors. *J. Alloys Compd.* **2017**, *695*, 2835–2843.
- (39) Jiang, Y.; Wang, Y.; Zeng, D.; Xiao, Y.; Wang, H.; Zhang, X.; Dai, X. Synthesis of bimetallic CoNi-CoNiO₂ nanoparticles embedded into mesoporous carbon as high-performance catalysts for supercapacitor electrode. *Microporous Mesoporous Mater.* **2018**, *272*, 222–231.
- (40) He, X.; Li, X.; Ma, H.; Han, J.; Zhang, H.; Yu, C.; Xiao, N.; Qiu, J. ZnO template strategy for the synthesis of 3D interconnected graphene nanocapsules from coal tar pitch as supercapacitor electrode materials. *J. Power Sources* **2017**, *340*, 183–191.
- (41) Lee, K. S.; Park, C. W.; Kim, J.-D. Synthesis of ZnO/activated carbon with high surface area for supercapacitor electrodes. *Colloids Surf., A* **2018**, *555*, 482–490.
- (42) Balasubramaniam, M.; Balakumar, S. Exploration of electrochemical properties of zinc antimonate nanoparticles as supercapacitor electrode material. *Mater. Sci. Semicond. Process.* **2016**, *56*, 287–294.
- (43) Saravananakumar, B.; Ravi, G.; Ganesh, V.; Ameen, F.; Al-Sabri, A.; Yuvakkumar, R. Surfactant assisted zinc doped tin oxide nanoparticles for supercapacitor applications. *J. Sol-Gel Sci. Technol.* **2018**, *86* (3), 521–535.
- (44) Wang, Q.; Zhu, L.; Sun, L.; Liu, Y.; Jiao, L. Facile synthesis of hierarchical porous ZnCo₂O₄ microspheres for high-performance supercapacitors. *J. Mater. Chem. A* **2015**, *3* (3), 982–985.
- (45) Xu, L.; Zhao, Y.; Lian, J.; Xu, Y.; Bao, J.; Qiu, J.; Xu, L.; Xu, H.; Hua, M.; Li, H. Morphology controlled preparation of ZnCo₂O₄ nanostructures for asymmetric supercapacitor with ultrahigh energy density. *Energy* **2017**, *123*, 296–304.
- (46) Bao, L.; Zang, J.; Li, X. Flexible Zn₂SnO₄/MnO₂ core/shell nanocable–carbon microfiber hybrid composites for high-performance supercapacitor electrodes. *Nano Lett.* **2011**, *11* (3), 1215–1220.
- (47) Jin, K.; Wang, Q.; Chen, L.; Lv, Z.; Xu, J.; Hong, B.; Wang, X. Zn₂SnO₄/activated carbon composites for high cycle performance supercapacitor electrode. *J. Alloys Compd.* **2018**, *767*, 419–423.